Corrosion Science 82 (2014) 173–179

Contents lists available at ScienceDirect

Corrosion Science

journal homepage: www.elsevier.com/locate/corsci

Eelectrochemical properties and corrosion resistance of carbon-ion-implanted magnesium

Ruizhen Xu, Xiongbo Yang, Penghui Li, Kai Wong Suen, Guosong Wu, Paul K. Chu *

Department of Physics and Materials Science, City University of Hong Kong, Tat Chee Avenue, Kowloon, Hong Kong, China

ARTICLE INFO

Article history:
Received 22 May 2013
Accepted 21 January 2014
Available online 30 January 2014

Keywords:
A. Magnesium
B. TEM
B. EIS
B. XPS
B. Ion implantation

ABSTRACT

The corrosion resistance of magnesium-based biomaterials is critical to clinical applications. In this work, carbon as a biocompatible and benign nonmetallic element with high chemical inertness is implanted into pure magnesium to improve the corrosion behavior. X-ray photoelectron spectroscopy (XPS), high-resolution transmission electron microscopy (HR-TEM), and Raman scattering reveal the formation of an amorphous carbon layer after ion implantation. Electrochemical studies demonstrate remarkable improvement in the corrosion resistance of magnesium in simulated body fluids (SBF) and Dulbecco's Modified Eagle Medium (DMEM).

1. Introduction

Magnesium and its alloys have mechanical properties that are more compatible with bone tissues than conventional biometals like stainless steels [1–3]. Furthermore, unlike passive metals such as titanium alloys and stainless steels, magnesium-based materials degrade spontaneously in the physiological environment thereby making implant removal after surgery unnecessary [4,5]. However, the degradation rate may be too fast to meet clinical needs, especially in the initial stage [6–8] and because the degradation procedure is dynamic, it is crucial to improve the surface corrosion resistance of magnesium and magnesium alloys.

Plasma immersion ion implantation (PIII) is an effective surface modification technique [9–11]. It has been shown that PIII enhances the biocompatibility and corrosion resistance enhancements of titanium alloys both *in vitro* and *in vivo* [12] and similar effects may be achieved on magnesium alloys. In fact, PIII of metallic ions including Al [13–15], Ti [14,16,17], Ta [18], Y [19], Ce [20], and Zr [14], gaseous ions such as N_2 [21], H_2O [22], O_2 [23], and H_2 [24]), and multiple ions including Cr–O [25,26] and Al–O [27]) have been proposed to suppress the fast degradation on magnesium and its alloys. In order to cater to clinical applications, the corrosion resistance of Mg must be improved while maintaining the surface biocompatibility as well as the mechanical characteristics after surface modification. Carbon has diverse structures and possesses beneficial chemical and physical properties such as high chemical inertness and tribological properties [28]. As a benign element to human beings, there are many carbon-based biomaterials with good biological properties, for instance, pyrolytic carbon [29,30] and diamond–like carbon [31,32]. Therefore, carbon ion implantation may be a good technique to enhance the corrosion resistance and biological characteristics of magnesium. In this work, carbon is plasma-implanted into magnesium and the surface properties and enhancement effects are investigated systematically.

2. Experimental details

The as-cast pure magnesium plate was cut into blocks with dimensions of 10 mm × 10 mm × 5 mm. The samples were mechanically polished by up to 1 μm alumina powder, ultrasonically cleaned in ethanol, and dried in air. Carbon ion implantation was carried out on an HEMII-80 ion implanter with a carbon cathodic arc source. The samples were implanted for 30 min at a terminal voltage of 20 kV and base pressure of 5×10^{-4} Pa.

Atomic force microscopy (AFM) was utilized to examine the morphology of the surface before and after carbon ion implantation. The surface mechanical properties were determined on an MTS nanoindentation instrument. Raman scattering was performed in air on a *LabRam HR* spectrometer (*Horiba Jobin Yvon*) equipped with an *Olympus BX41* microscope and an Ar^+ laser (green line at 2.41 eV or 514.5 nm). The elemental depth profiles and chemical states were determined by X-ray photoelectron spectroscopy (XPS, Physical Electronics PHI 5802). Al Kα irradiation was employed and the estimated sputtering rate was 6 nm min^{-1} based on a reference standard. The microstructure and composition were probed by high-resolution transmission electron microscopy (HRTEM, JEM-2010F) and energy-dispersive X-ray spectroscopy (EDS, Oxford INCA 200).

* Corresponding author.
E-mail address: paul.chu@cityu.edu.hk (P.K. Chu).

0010-938X/$ - see front matter © 2014 Elsevier Ltd. All rights reserved.
http://dx.doi.org/10.1016/j.corsci.2014.01.015

The electrochemical corrosion characteristics were evaluated on a Zahner Zennium electrochemical workstation based on the conventional three-electrode technique in simulated body fluids (SBF) [33] and Dulbecco's Modified Eagle Medium (DMEM, GIBCO, cat. no. 12100-046) [34] at 37 °C. The SBF solution containing inorganic ions with concentrations (in mM) similar to those in human extracellular fluids (142.0 Na^+, 5.0 K^+, 1.5 Mg^{2+}, 2.5 Ca^{2+}, 147.8 Cl^-, 4.2 HCO_3^-, 1.0 HPO_4^{2-}, 0.5 SO_4^{2-} with a pH of 7.40) was prepared by dissolving reagent grade (in mM) 137.4914 NaCl, 4.2258 $NaHCO_3$, 3.0181 KCl, 1.0122 $K_2HPO_4{\cdot}3H_2O$, 1.5297 $MgCl_2{\cdot}6H_2O$, 2.6311 $CaCl_2$, and 0.5068 Na_2SO_4 in distilled water and buffered at pH 7.4 with 50.5035 mM trishydroxymethyl aminomethane (TRIS) and 1.0 M HCl. The DMEM cell culture medium was prepared by DMEM powder and the constituents were (in mM): 0.4 glycine, 0.39810428 L-arginine hydrochloride, 0.20127796 L-cystine 2HCl, 4 L-glutamine, 0.2 L-histidine hydrochloride·H_2O, 0.8015267 L-isoleucine, 0.8015267 L-leucine, 0.7978142 L-Lysine hydrochloride, 0.20134228 L-methionine, 0.4 L-phenylalanine, 0.4 L-serine, 0.79831934 L-threonine, 0.078431375 L-tryptophan, 0.39846742 L-tyrosine disodium salt dihydrate, 0.8034188 L-valine, 0.028571429 choline chloride, 0.008385744 D-calcium pantothenate, 0.009070295 folic Acid, 0.032786883 niacinamide, 0.019607844 pyridoxine hydrochloride, 0.00106383 riboflavin, 0.011869436 thiamine hydrochloride, 0.04 i-inositol, 1.8018018 $CaCl_2$, 2.48×10^{-4} $Fe(NO_3)_3{\cdot}9H_2O$, 0.8139166 $MgSO_4$, 5.3333335 KCl, 110.344826 NaCl, 0.9057971 $NaH_2PO_4{\cdot}H_2O$, 25 dextrose, and 0.039851222 phenol red. The potential was referenced to a saturated calomel electrode (SCE) and the counter electrode was a platinum sheet. The working electrode was mounted with silicone to expose an area of 10 mm × 10 mm. The EIS data were collected from 100 kHz to 100 mHz with a 5 mV sinusoidal perturbation signal. The polarization curves were acquired at a scanning rate 2 mV s^{-1} right after the EIS tests and the corrosion morphologies after the electrochemical tests were examined by scanning electron microscopy (SEM, FEI/Philips XL30 Esem-FEG).

3. Results and discussion

The atomic force microscopy (AFM) images of the untreated Mg and carbon-implanted Mg in Fig. 1 are quite different. The untreated sample has uniformly distributed and small cones with scratches produced during mechanical polishing (Fig. 1a). On the other hand, Fig. 1b shows that the surface of carbon–implanted Mg has large dome shaped islands and more distinguished scratches. The root-mean-square (RMS) roughness values of the untreated Mg and treated Mg are 6.43 and 5.15 nm, respectively. A smoother surface was obtained after ion implantation probably due to surface restructuring at elevated temperature during implantation [11,35].

As shown in Fig. 2, there are no significant changes in the hardness and elastic modulus between the implanted and unimplanted samples. The reproducibility of the nanoindentation measurements is determined by repeating the tests four times and the error bar represents one standard deviation. The modulus after carbon ion implantation increases from 36 GPa to 40 GPa but the hardness diminishes slightly from 0.64 GPa to 0.52 GPa. Although higher hardness has been reported from DLC coatings [36], our data disclose that the hardness and modulus after implantation are similar to those of the unimplanted sample. The results are actually quite desirable because the favorable surface mechanical properties of magnesium are maintained after carbon PIII.

The Raman scattering spectra acquired from the carbon–implanted magnesium in Fig. 3 shows the typical pattern of amorphous carbon (a-C films). The most common Raman spectra fitting method is to employ two Gaussian peaks with linear background subtraction with the G peak centered at around 1540–1580 cm^{-1} and D peak centered around 1350 cm^{-1} [36]. It is based on the assumption that the amorphous carbon films are composed of sp^2 and sp^3 networks. In this study, the Raman spectrum can be deconvoluted into two sub-peaks: G peak at 1554.4 cm^{-1} and D peak at 1381.9 cm^{-1}. Similar Raman spectra have been obtained from DLC coatings on Mg alloys [36,37]. The D peak can be ascribed to the evolution to nano-crystalline graphite accompanied by conversion of sp^3 bonds to sp^2 bonds [37].

The XPS depth profiles obtained from the implanted sample is depicted in Fig. 4. The concentrations of carbon, magnesium, and oxygen, change gradually with depth in the implanted sample. The surface oxygen stems from surface contamination and spontaneously oxidation due to the non-ultra-high-vacuum (UHV) conditions [28]. The carbon concentration drops quickly from 80% initially to about 10% after sputtering for 4 min and the low C concentration diminishes slowly throughout a depth of about 34 nm. The carbon-containing layer is therefore inferred to be about 58 nm thick.

The common chemical bonds in amorphous and nanocrystalline carbon are sp^3 and sp^2 hybridizations and XPS can reveal the C binding energy and discern the sp^3 and sp^2 bonds. In the sp^3 configuration, a carbon atom forms four sp^3 orbitals and makes a strong σ bond to the adjacent atom. In the sp^2 configuration, a carbon atom forms three sp^2 orbitals and forms three σ bonds and the remaining p orbital forms a π bond. Fig. 5a depicts the C 1s spectra at different sputtering time showing the C 1s peak has both sp^2 and sp^3 components. The peak at a binding energy of 284.3 eV is attributed to sp^2 carbon atoms whereas that 285.3 eV is due to sp^3 carbon atoms. A large sp^3 content in excess of 80% is associated with high hardness [11]. In our samples, owing to relatively small sp^3 content, the hardness before and after carbon ion implantation does not change much. The high fraction of sp^2

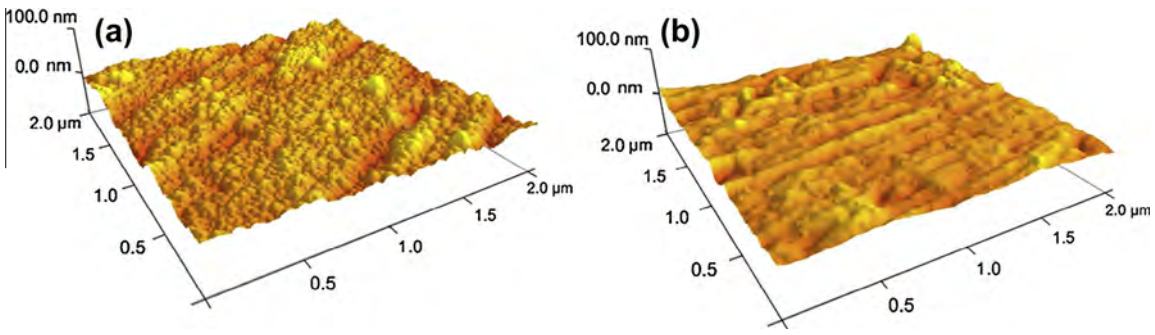

Fig. 1. Surface morphologies obtained by atomic force microscopy (AFM): (a) untreated Mg and (b) carbon-implanted Mg.

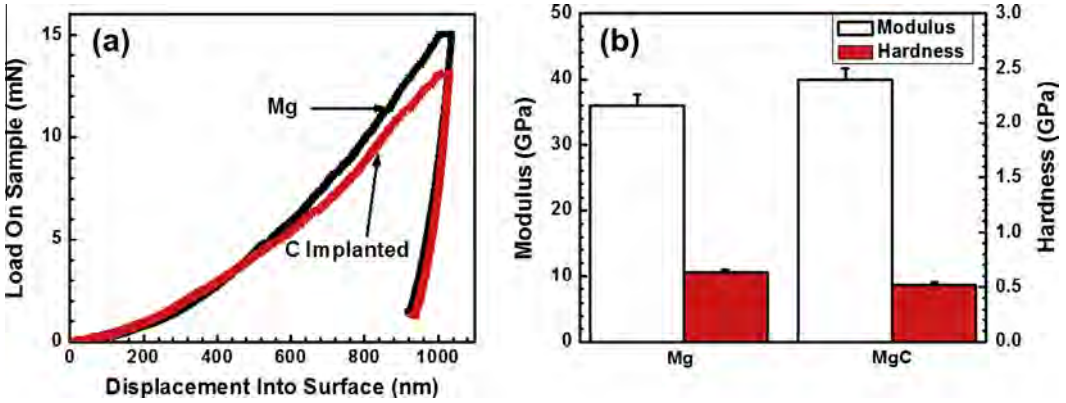

Fig. 2. (a) Load on sample as a function of displacement into surface and (b) hardness and elastic modulus values of Mg and carbon–implanted Mg.

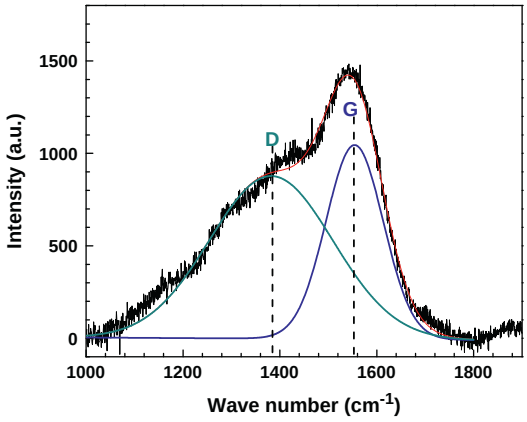

Fig. 3. Raman scattering spectrum of the carbon–implanted magnesium.

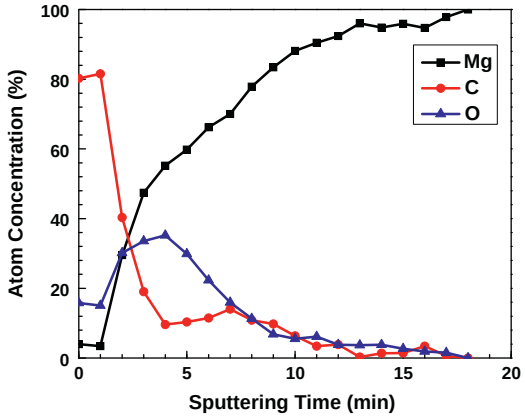

Fig. 4. XPS elemental depth profile of the carbon–implanted magnesium.

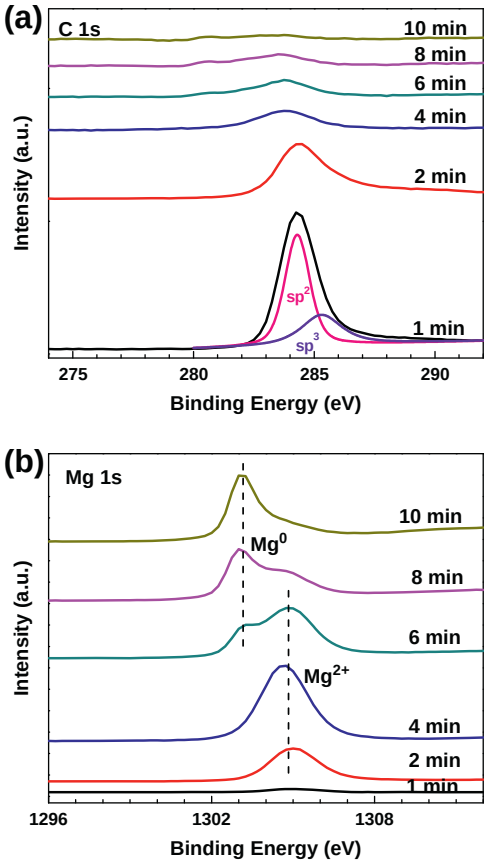

Fig. 5. High-resolution XPS spectra of the carbon-ion-implanted Mg obtained at different sputtering time: (a) C 1s and (b) Mg 1s.

carbon may result from the low implantation voltage. The carbon ions do not have enough energy to penetrate the surface and instead stick to the surface in their lowest energy state with sp^2 hybridization. Zou [38] has proposed that sp^2 can morph into sp^3 if the carbon ion energy is increased, but excessively high energy can also reduce the sp^3 content due to thermal relaxation.

As shown in Fig. 5b, the Mg 1s peak shifts from the oxidized state (Mg^{2+}) to the metallic state (Mg^0) with depth. According to previous studies, an oxide layer is formed on the surface of sample after ion implantation. However, this magnesium oxide film does not play a key role in enhancing the corrosion resistance because aggressive ions can penetrate this layer to attack the substrate [39]. After carbon implantation, the surface of the implanted sample is composed of carbon and magnesium oxide.

Fig. 6 is the high-resolution transmission electron microscopy (HR-TEM) image obtained from the surface of the carbon–implanted magnesium. The spacings between the lattice planes in area A and area B are 0.21 nm and 0.28 nm, respectively, corresponding to the (200) and (001) planes of MgO [40,41]. There is no obvious lattice in area C thus suggesting an amorphous structure. The bar chart presents the average results of 5 measurements by EDS (energy-dispersive X-ray spectroscopy) from area C. Area C

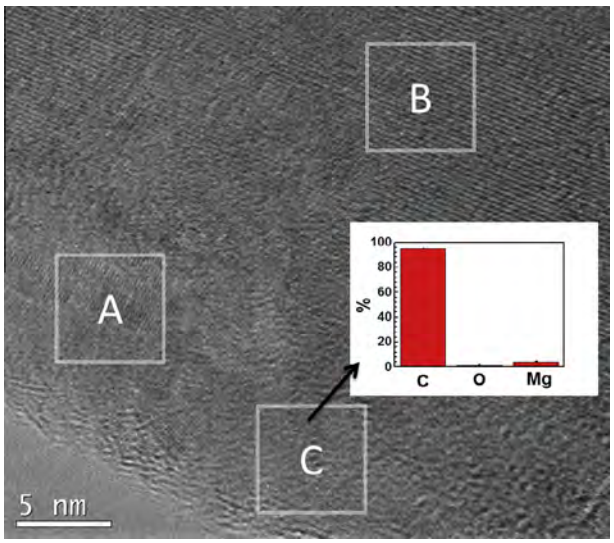

Fig. 6. HR-TEM image of surface of carbon implanted sample together with the element composition in area C (inset).

is mainly composed of carbon (94.95%) and confirms the amorphous structure.

Fig. 7a and b displays the polarization curves of the samples soaked in DMEM and SBF, respectively. Generally, the anodic region describes dissolution of the sample at an elevated potential and the cathodic polarization curve represents cathodic hydrogen evolution *via* the water reduction reaction. Here, the anodic polarization curves do not clearly indicate a Tafel region and hence, the corrosion potential and corrosion current density are derived directly from the cathodic polarization curves. The cathodic Tafel slope (β_c) is derived from the fitted linear region. After the slope is obtained, it can be extrapolated back to the open-circuit corrosion potential (E_{corr}) to obtain the corrosion current density (i_{corr}), as illustrated in Fig. 7. The E_{corr}, i_{corr}, and β_c values determined from the polarization curves are listed in Table 1. The β_c values of all the samples are similar with the exception of a smaller β_c for the implanted sample in DMEM, indicating that the implanted sample undergoes a slower electrochemical reaction in DMEM. The curves obtained from the implanted magnesium shift to lower current densities and higher potentials in both simulated solutions. The corrosion potential of the implanted sample increases from −1.98 V to −1.71 V in DMEM and from −1.98 V to −1.94 V in SBF. The corrosion current densities decrease from 6.52×10^{-5} A cm^{-2} to 1.88×10^{-6} A cm^{-2} in DMEM and from 2.58×10^{-4} A cm^{-2} to 2.63×10^{-5} A cm^{-2} in SBF after carbon PIII. Suppression of both the cathodic and anodic reactions shifts the polarization curves towards lower current densities. Generally, the smaller the corrosion current density, the lower is the corrosion rate [42,43]. The polarization characteristics reveal that degradation of Mg is improved after carbon ion implantation. On account of the formation of a corrosion resistant layer of albumin in the cell culture medium [44], the corrosion current density in DMEM is lower than that in SBF.

Electrochemical impedance spectroscopy is used to evaluate the corrosion resistance and analyze the corrosion mechanism. The results are presented in Fig. 8. In the Nyquist plots shown in Fig. 8a and d, the capacitive loop of the treated sample is obviously enlarged compared to the untreated sample in both solutions. Usually, the capacitive loops are attributed to charge transfer, film effects, and mass transfer in the corrosion product layer [39,45]. The Bode plots of the impedance versus frequency are presented in Fig. 8b and e. Within the range of our investigation, the impedance of the carbon-implanted sample at any frequency is higher than that of the unimplanted sample. At a higher frequency (100 kHz), the impedance of the implanted Mg in DMEM (25.7 ohm cm^2) is slightly higher than that of the unimplanted Mg (21 ohm cm^2). Similar results are found from SBF. The impedance of the carbon ion-implanted Mg in SBF is 23 ohm cm^2, which is slightly larger than that of the unimplanted Mg (16 ohm cm^2). The higher impedance at a higher frequency indicates the inability of electrolyte ions to penetrate the implanted layer on the surface. At a lower frequency (100 mHz), the impedance determined from the carbon–implanted Mg is more than 10 times larger than that of the unimplanted Mg in both solutions. In DMEM, the impedance of the carbon implanted Mg is 37,624 ohm cm^2 and that of the unimplanted Mg is 2608 ohm cm^2. In SBF, the impedance values of the implanted and the unimplanted samples are 964 ohm cm^2 and 79 ohm cm^2, respectively. This is because the carbon-containing surface layer mitigates the charge transfer process. The Bode impedance plots indicate the implanted Mg has higher corrosion resistance. The Bode phase plots are shown in Fig. 8c and e. The phase angle evolution is also altered after carbon PIII. In DMEM, the unimplanted Mg shows a phase angle maximum of 51 at 34 Hz whereas the carbon implanted Mg exhibits a phase angle maximum of 73 at 2099 Hz. In SBF, the phase angle maximum of the unimplanted Mg and implanted Mg are 27 and 65 at 340 Hz and 3306 Hz, respectively. Moreover, the carbon-implanted sample shows the phase angle maximum over a wide range of frequency compared to the Mg in the two solutions. The occurrence of a constant phase angle maximum over a wide range of frequencies is typical of a passive surface and indicates a near capacitive

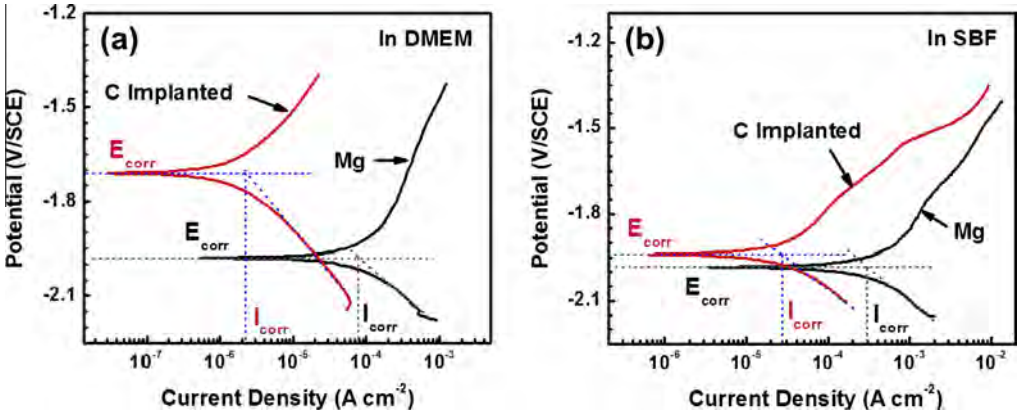

Fig. 7. Polarization curves of Mg and carbon-implanted Mg in different media: (a) DMEM and (b) SBF.

Table 1
i_{corr}, E_{corr} and β_c determined from the polarization curves.

Sample	In DMEM		In SBF	
	Mg	C Implanted Mg	Mg	C Implanted Mg
E_{corr} (V/SCE)	−1.98	−1.71	−1.98	−1.94
i_{corr} (A cm^{-2})	6.52×10^{-5}	1.88×10^{-6}	2.58×10^{-4}	2.63×10^{-5}
β_c (V decade^{-1})	−0.20	−0.28	−0.23	−0.21

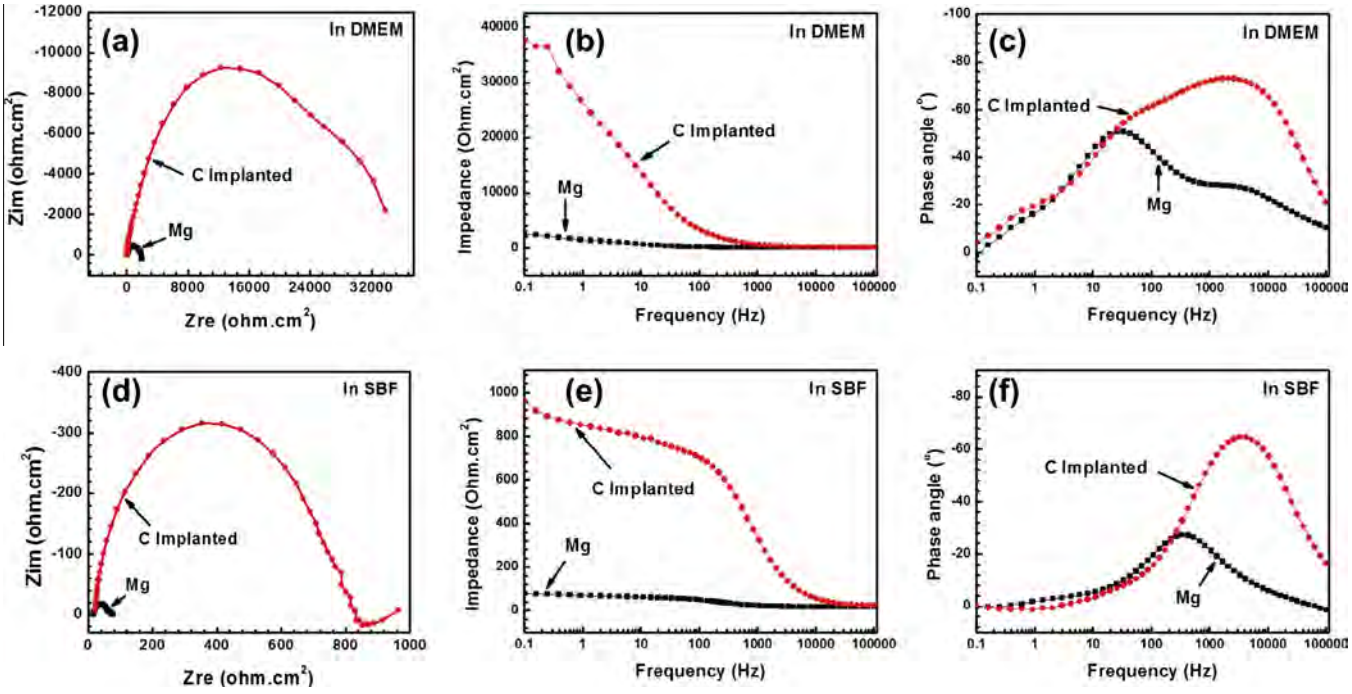

Fig. 8. EIS curves of samples in DMEM and SBF: (a) Nyquist plots in DMEM, (b) Bode plots of impedance versus frequency in DMEM, (c) Bode plots of phase angle versus frequency in DMEM, and (d) Nyquist plots in SBF, (e) Bode plots of impedance versus frequency in SBF, and (f) Bode plots of phase angle versus frequency in SBF.

behavior. The difficulty in charge transfer ascertains good corrosion protection ability of the implanted Mg. The Bode impedance and Bode phase angle plots further corroborate the observations from the Nyquist plot. These results are consistent with the polarization tests.

To analyze the physical structure of the electrode system and impedance response, equivalent circuits are used to describe the electrochemical interface between the samples and solutions, as shown in Fig. 9. Here, R_s is the solution resistance between the reference and working electrodes, CPE_f is the capacitance of the deposited film, R_{pore} is the sum of the resistance of all the pores in the corrosion product, CPE_{dl} is the electrical double-layer capacitance at the substrate/electrolyte inerface, R_t is the charge transfer resistance of the substrate, CPE_{diff} is the capacitance pertaining to diffusion, and R_{diff} is the corresponding resistance. Zhao et al. [46], Jamesh et al. [47] and the previous study [48] have used a similar model of $R_s(R_tCPE_{dl})(R_{diff}CPE_{diff})$ to explain the corrosion behavior of the bare Mg alloy. The model of $R_s(CPE_f(R_{pore}(CPE_{dl}(R_t(CPE_{diff}R_{diff})))))$ for the implanted Mg was proved to be possessed better barrier property against the diffusion of corrosion products [49]. The fitted EIS data are presented in Table 2. The value of R_s depends on the conductivity of the medium as well as cell geometry which is small and similar in all the tests and is thus neglected here. R_p represents the polarization resistance, which is the sum of R_t and R_{diff} in Fig. 9a and the sum of R_{pore}, R_t, and R_{diff} in Fig. 9b. In general, materials that show higher resistance offer better corrosion resistance and vice versa. The smaller R_p values observed from the unimplanted Mg indicate that the corrosion rates are rapid in

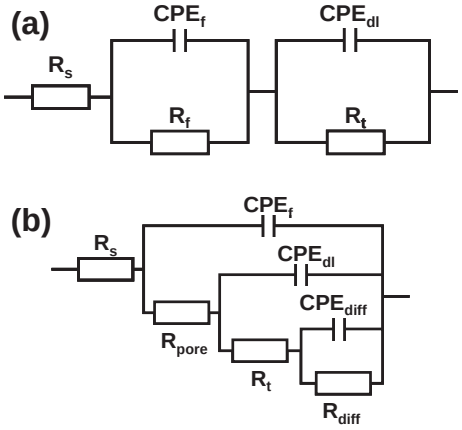

Fig. 9. Equivalent circuits based on analysis of the EIS spectra: (a) Mg and (b) C implanted Mg.

both solutions. On the contrary, R_p is higher after C ion implantation, suggesting that the corrosion rates are retarded in DMEM and SBF due to the graphite barrier layer.

Fig. 10 displays the corroded surfaces of the unimplanted and carbon–implanted Mg samples after electrochemical tests in SBF and DMEM. Severe corrosion cracks (Fig. 10a and c) are present on the unimplanted Mg surface while the carbon-implanted Mg

Table 2
Fitted EIS data.

Sample	In DMEM		In SBF	
	Mg	C Implanted Mg	Mg	C Implanted Mg
Y_{of} (Ω^{-2} cm^{-2} s^{-n})	–	6.955×10^{-7}	–	1.304×10^{-6}
n_f	–	0.9238	–	0.6463
R_{pore} (Ω cm^2)	–	2836	–	19.23
Y_{odl} (Ω^{-2} cm^{-2} s^{-n})	2.761×10^{-5}	2.194×10^{-6}	8.994×10^{-3}	6.311×10^{-7}
n_{dl}	0.6792	0.7146	0.9349	0.934
R_t (Ω cm^2)	79.26	23,930	9.117	737.4
Y_{odiff} (Ω^{-2} cm^{-2} s^{-n})	6844×10^{-5}	4.999×10^{-5}	8.277×10^{-5}	1.779×10^{-4}
n_{diff}	0.7228	0.9999	0.7988	0.8637
R_{diff} (Ω cm^2)	1723	5874	47.39	80.67

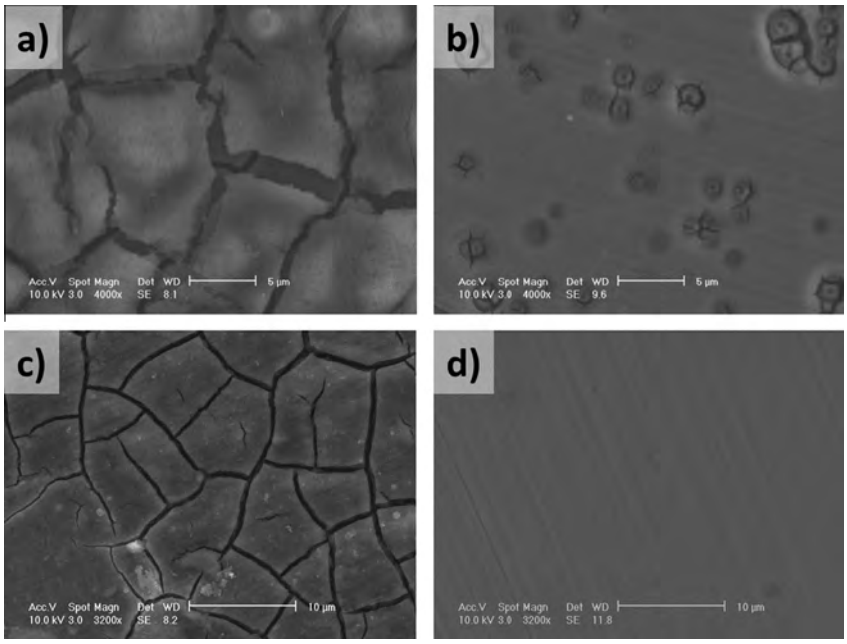

Fig. 10. Surface morphology of magnesium after electrochemical tests: (a) Mg in SBF, (b) carbon–implanted Mg in SBF, (c) Mg in DMEM, and (d) carbon–implanted Mg in DMEM.

suffers less corrosive attack (Fig. 10b) and no obvious attack (Fig. 10d). The results suggess physical and chemical changes at the interface between the Mg and solutions. In comparison, the carbon–implanted Mg has a more electrochemically stable surface and the results are consistent with those of the electrochemcial tests.

4. Conclusion

A surface layer composed of amorphous graphite is formed in magnesium by carbon plasma immersion ion implantation. The shift in E_{corr} to the more noble direction and significant reduction in the current density (i_{corr}) observed from the carbon PIII Mg indicate enhanced corrosion resistance in SBF and DMEM. The EIS curves further confirm the better electrochemical stability of the carbon–implanted Mg samples. Our results suggest that C PIII is a feasible technique to enhance the corrosion resistane of Mg in both SBF and DMEM and the technique can be expected to expedite potential clinical applications of Mg-based biodegradable surgical devices.

Acknowledgments

This work was financially supported by Hong Kong Research Grants Council (RGC), General Research Funds (GRF) Nos. CityU 112510 and 112212 as well as City University of Hong Kong Applied Research Grant (ARG) Nos. 9667066 and 9667069.

References

[1] E.L. Zhang, L. Yang, J.W. Xu, H.Y. Chen, Microstructure, mechanical properties and bio-corrosion properties of Mg–Si(–Ca, Zn) alloy for biomedical application, Acta Biomater. 6 (2010) 1756–1762.
[2] B. Zberg, P.J. Uggowitzer, J.F. Loffler, MgZnCa glasses without clinically observable hydrogen evolution for biodegradable implants, Nat. Mater. 8 (2009) 887–891.
[3] X.N. Gu, Y.F. Zheng, Y. Cheng, S.P. Zhong, T.F. Xi, In vitro corrosion and biocompatibility of binary magnesium alloys, Biomaterials 30 (2009) 484–498.
[4] M.P. Staiger, A.M. Pietak, J. Huadmai, G. Dias, Magnesium and its alloys as orthopedic biomaterials: a review, Biomaterials 27 (2006) 1728–1734.
[5] C. Castellani, R.A. Lindtner, P. Hausbrandt, E. Tschegg, S.E. Stanzl-Tschegg, G. Zanoni, S. Beck, A.M. Weinberg, Bone-implant interface strength and osseointegration: biodegradable magnesium alloy versus standard titanium control, Acta Biomater. 7 (2011) 432–440.
[6] G. Baril, N. Pebere, The corrosion of pure magnesium in aerated and deaerated sodium sulphate solutions, Corros Sci. 43 (2001) 471–484.
[7] F.J. Medel, J.A. Puertolas, Wear resistance of highly cross-linked and remelted polyethylenes after ion implantation and accelerated ageing, Proc. Inst. Mech. Eng. H 222 (2008) 877–885.
[8] J. Chen, J.Q. Wang, E.H. Han, J.H. Dong, W. Ke, States and transport of hydrogen in the corrosion process of an AZ91 magnesium alloy in aqueous solution, Corros. Sci. 50 (2008) 1292–1305.
[9] J.R. Conrad, J.L. Radtke, R.A. Dodd, F.J. Worzala, N.C. Tran, Plasma source ion-implantation technique for surface modification of materials, J. Appl. Phys. 62 (1987) 4591–4596.

[10] P.K. Chu, B.Y. Tang, Y.C. Cheng, P.K. Ko, Principles and characteristics of a new generation plasma immersion ion implanter, Rev. Sci. Instrum. 68 (1997) 1866–1874.
[11] P.K. Chu, J.Y. Chen, L.P. Wang, N. Huang, Plasma-surface modification of biomaterials, Mater. Sci. Eng. R 36 (2002) 143–206.
[12] Y. Zhao, S.M. Wong, H.M. Wong, S.L. Wu, T. Hu, K.W.K. Yeung, P.K. Chu, Effects of carbon and nitrogen plasma immersion ion implantation on in vitro and in vivo biocompatibility of titanium alloy, ACS Appl. Mater. Int. 5 (2013) 1510–1516.
[13] M.K. Lei, P. Li, H.G. Yang, X.M. Zhu, Wear and corrosion resistance of Al ion implanted AZ31 magnesium alloy, Surf. Coat. Technol. 201 (2007) 5182–5185.
[14] C.L. Liu, Y.C. Xin, X.B. Tian, P.K. Chu, Corrosion behavior of AZ91 magnesium alloy treated by plasma immersion ion implantation and deposition in artificial physiological fluids, Thin Solid Films 516 (2007) 422–427.
[15] G.S. Wu, R.Z. Xu, K. Feng, S.L. Wu, Z.W. Wu, G.Y. Sun, G. Zheng, G.Y. Li, P.K. Chu, Retardation of surface corrosion of biomedical magnesium alloys by aluminum ion implantation, Appl. Surf. Sci. 258 (2012) 7651–7657.
[16] F. Chen, H. Zhou, S. Cai, F.X. Lv, C.M. Li, Corrosion resistance properties of AZ31 magnesium alloy after Ti ion implantation, Rare Met. 26 (2007) 142–146.
[17] C.G. Liu, Y.C. Xin, X.B. Tian, J. Zhao, P.K. Chu, Corrosion resistance of titanium ion implanted AZ91 magnesium alloy, J. Vac. Sci. Technol. A 25 (2007) 334–339.
[18] X.M. Wang, X.Q. Zeng, G.S. Wu, S.S. Yao, Y.J. Lai, Effects of tantalum ion implantation on the corrosion behavior of AZ31 magnesium alloys, J. Alloys Compd. 437 (2007) 87–92.
[19] X.M. Wang, X.Q. Zeng, G.S. Wu, S.S. Yao, The effect of Y-ion implantation on the oxidation of AZ31 magnesium alloy, Mater. Lett. 61 (2007) 968–970.
[20] X.M. Wang, X.Q. Zeng, S.S. Yao, G.S. Wu, Y.J. Lai, The corrosion behavior of Ce-implanted magnesium alloys, Mater. Charact. 59 (2008) 618–623.
[21] X.B. Tian, C.B. Wei, S.Q. Yang, R.K.Y. Fu, P.K. Chu, Corrosion resistance improvement of magnesium alloy using nitrogen plasma ion implantation, Surf. Coat. Technol. 198 (2005) 454–458.
[22] X.B. Tian, C.B. Wei, S.Q. Yang, R.K.Y. Fu, P.K. Chu, Water plasma implantation/oxidation of magnesium alloys for corrosion resistance, Nucl. Instrum. Methods B 242 (2006) 300–302.
[23] G.J. Wan, M.F. Maltz, H. Sun, P.P. Li, N. Huang, Corrosion properties of oxygen plasma immersion ion implantation treated magnesium, Surf. Coat. Technol. 201 (2007) 8267–8272.
[24] A. Bakkar, V. Neubert, Improving corrosion resistance of magnesium-based alloys by surface modification with hydrogen by electrochemical ion reduction (EIR) and by plasma immersion ion implantation (PIII), Corros. Sci. 47 (2005) 1211–1225.
[25] R.Z. Xu, G.S. Wu, X.B. Yang, T. Hu, Q.Y. Lu, P.K. Chu, Controllable degradation of biomedical magnesium by chromium and oxygen dual ion implantation, Mater. Lett. 65 (2011) 2171–2173.
[26] R.Z. Xu, G.S. Wu, X.B. Yang, X.M. Zhang, Z.W. Wu, G.Y. Sun, G.Y. Li, P.K. Chu, Corrosion behavior of chromium and oxygen plasma-modified magnesium in sulfate solution and simulated body fluid, Appl. Surf. Sci. 258 (2012) 8273–8278.
[27] G.S. Wu, K. Feng, A. Shanaghi, Y. Zhao, R.Z. Xu, G.Y. Yuan, P.K. Chu, Effects of surface alloying on electrochemical corrosion behavior of oxygen-plasma-modified biomedical magnesium alloy, Surf. Coat. Technol. 206 (2012) 3186–3195.
[28] Biodegradable plastics from corn starch and sugar, Int. Sugar J. 113 (2011). 86-86.
[29] E. Cenni, D. Granchi, C.R. Arciola, G. Ciapetti, L. Savarino, S. Stea, D. Cavedagna, A. Dileo, A. Pizzoferrato, Adhesive protein expression on endothelial-cells after contact in-vitro with polyethylene terephthalate coated with pyrolytic carbon, Biomaterials 16 (1995) 1223–1227.
[30] L. Ma, G. Sines, Fatigue behavior of a pyrolytic carbon, J. Biomed. Mater. Res. 51 (2000) 61–68.
[31] L.A. Thomson, F.C. Law, N. Rushton, J. Franks, Biocompatibility of diamond-like carbon coating, Biomaterials 12 (1991) 37–40.
[32] S. Linder, W. Pinkowski, M. Aepfelbacher, Adhesion, cytoskeletal architecture and activation status of primary human macrophages on a diamond-like carbon coated surface, Biomaterials 23 (2002) 767–773.
[33] T. Kokubo, H. Takadama, How useful is SBF in predicting in vivo bone bioactivity?, Biomaterials 27 (2006) 2907–2915
[34] R. Dulbecco, G. Freeman, Plaque production by the polyoma virus, Virology 8 (1959) 396–397.
[35] L. Shichang, Z. Zhaoyang, G. Shaobin, L. Hongxia, W. Dongdong, Mutation-screening in l-(+)-lactic acid producing strains by ion implantation, Indian J. Microbiol. 51 (2011) 138–143.
[36] R. Bavadi, S. Valedbagi, Physical properties of titanium nitride thin film prepared by DC magnetron sputtering, Mater. Phys. Mech. 15 (2012) 167–172.
[37] L.H. Li, H.Q. Zhang, Y.H. Zhang, P.K. Chu, X.B. Tian, L.F. Xia, X.X. Ma, Structural analysis of arc deposited diamond-like carbon films by Raman and X-ray photoelectron spectroscopy, Mater. Sci. Eng. B – Solid 94 (2002) 95–101.
[38] Y.S. Zou, Y.F. Wu, H. Yang, K. Cang, G.H. Song, Z.X. Li, K. Zhou, The microstructure, mechanical and friction properties of protective diamond like carbon films on magnesium alloy, Appl. Surf. Sci. 258 (2011) 1624–1629.
[39] Y.C. Xin, T. Hu, P.K. Chu, Degradation behaviour of pure magnesium in simulated body fluids with different concentrations of HCO_3^-, Corros. Sci. 53 (2011) 1522–1528.
[40] J.H. Nordlien, S. Ono, N. Masuko, K. Nisancioglu, A TEM investigation of naturally formed oxide films on pure magnesium, Corros. Sci. 39 (1997) 1397–1414.
[41] B. Yoo, K.J. Kim, Y.H. Kim, K. Kim, M.J. Ko, W.M. Kim, N.G. Park, Titanium nitride thin film as a novel charge collector in TCO-less dye-sensitized solar cell, J. Mater. Chem. 21 (2011) 3077–3084.
[42] Z.G. Xie, A.M. Allen, M. Chang, P. Wang, T.J. Gung, Control of bombardment energy and energetic species toward a superdense titanium nitride film, J. Vac. Sci. Technol. A 28 (2010) 1326–1329.
[43] Y.Q. Chen, F.Y. Gao, H.Y. Peng, H.W. Jiang, L.C. Yin, D. Wang, H.L. Huang, Deposition of titanium nitride film on Mg–Li alloys by DC reactive magnetron sputtering, Adv. Res. Ind., Inf. Syst. Mater. Eng., Pts 1–7 (204–210) (2011) 1685–1690.
[44] J.X. Xue, G.J. Zhang, F.F. Xu, H.B. Zhang, X.G. Wang, S.M. Peng, X.G. Long, Lattice expansion and microstructure evaluation of Ar ion-irradiated titanium nitride, Nucl. Instrum. Methods B 308 (2013) 62–67.
[45] Q. Qu, J. Ma, L. Wang, L. Li, W. Bai, Z.T. Ding, Corrosion behaviour of AZ31B magnesium alloy in NaCl solutions saturated with CO(2), Corros. Sci. 53 (2011) 1186–1193.
[46] Y. Zhao, G.S. Wu, J. Jiang, H.M. Wong, K.W.K. Yeung, P.K. Chu, Improved corrosion resistance and cytocompatibility of magnesium alloy by two-stage cooling in thermal treatment, Corros. Sci. 59 (2012) 360–365.
[47] M. Jamesh, G.S. Wu, Y. Zhao, P.K. Chu, Effects of silicon plasma ion implantation on electrochemical corrosion behavior of biodegradable Mg-Y-RE alloy, Corros. Sci. 69 (2013) 158–163.
[48] R.Z. Xu, X.B. Yang, K.W. Suen, G.S. Wu, P.H. Li, P.K. Chu, Effects of chromium ion implantation voltage on the corrosion resistance and cytocompatibility of dual chromium and oxygen plasma-ion-implanted biodegradable magnesium, Surf. Coat. Technol. 235 (2013) 875–880.
[49] X. Guo, K. Du, Q. Guo, Y. Wang, R. Wang, F. Wang, Effect of phytic acid on the corrosion inhibition of composite film coated on Mg–Gd–Y alloy, Corros. Sci. 76 (2013) 129–141.